NEUTRON STARS:
COSMIC SUPERFLUIDS

RTG Colloquium
July 1, 2020

Dr Vanessa Graber
Institute for Space Sciences

ICE

Contents

Contents

Neutron Stars — Structure

- The interior structure is complex and influenced by the (unknown) equation of state. However, there is a **canonical understanding**.
- After $\sim 10^4$ years neutron stars are in equilibrium and have temperatures of $10^6 - 10^8\,\mathrm{K}$. They are composed of **distinct layers**.
- For our purposes, we separate neutron stars into a **solid crust** and a **fluid core**, containing three distinct superfluid components.

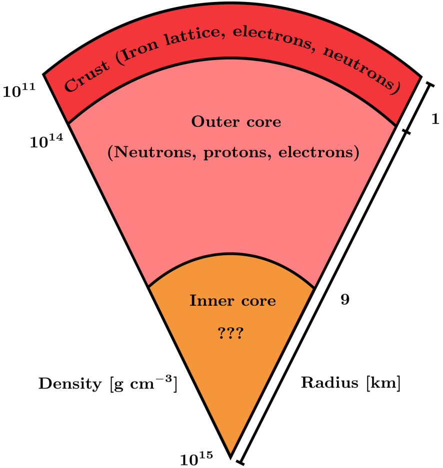

Figure 1: Sketch of the neutron star interior.

- Neutron stars are hot compared to low-temperature experiments on Earth, but cold in terms of their nuclear physics (Migdal, 1959).
- Neutrons and protons are **fermions** and can become unstable to **Cooper pair formation** due to an attractive contribution to the nucleon-nucleon interaction potential.
- The pairing process is described within the standard microscopic **BCS** theory of superconductivity (Bardeen, Cooper & Schrieffer, 1957).
- Compare the equilibrium to the nucleons' **Fermi temperature**:

$$T_{\mathrm{F}} = k_{\mathrm{B}}^{-1} E_{\mathrm{F}} \sim 10^{12}\,\mathrm{K} \gg 10^{6} - 10^{8}\,\mathrm{K}. \tag{1}$$

Neutron star matter is strongly influenced by quantum mechanics!

Phase transition temperatures

- Detailed BCS calculations provide the pairing gaps Δ, which are associated with the **critical temperatures** T_c for the superfluid and superconducting phase transitions.

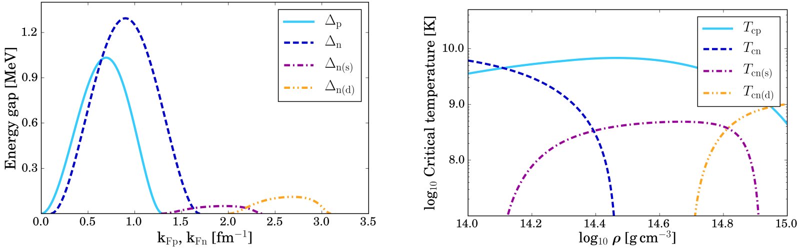

Figure 2: Left: Parametrised proton (singlet) and neutron (singlet, triplet) energy gaps as a function of Fermi wave numbers (Ho, Glampedakis & Andersson, 2012). Right: Critical temperatures of superconductivity/superfluidity as a function of the neutron star density. The values are computed for the NRAPR equation of state (Steiner et al., 2005; Chamel, 2008).

Contents

Basics

- Superfluids flow **without viscosity**, while superconductors have vanishing electrical conductivity and exhibit **Meissner effect**.
- Both states involve large numbers of particles condensed into the same quantum state, characteristic for **macroscopic quantum phenomena**.
- Most of our understanding of superfluidity and superconductivity in neutron stars originates from **laboratory counterparts**.

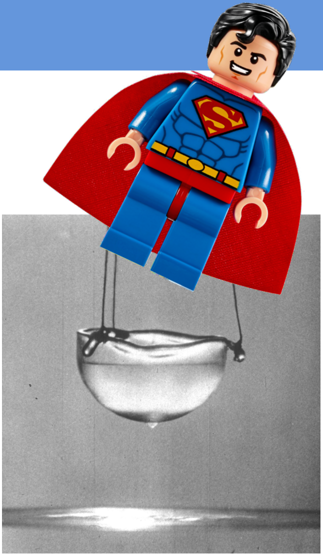

Figure 3: Superfluid helium creeps up the walls to eventually empty the bucket.

Quantised vorticity

- Superfluids can be characterised by **macroscopic wave functions** $\Psi = \Psi_0 \, e^{i\varphi}$ that satisfy the Schrödinger equation. Using standard QM formalism, one can determine a **superfluid velocity**

$$\boldsymbol{v}_{\mathrm{S}} \equiv \frac{\boldsymbol{j}_{\mathrm{S}}}{\rho_{\mathrm{S}}} = \frac{\hbar}{m_{\mathrm{c}}} \nabla\varphi, \qquad \Rightarrow \qquad \boldsymbol{\omega} \equiv \nabla \times \boldsymbol{v}_{\mathrm{S}} = 0. \tag{2}$$

Figure 4: Envisage vortices as tiny, rotating tornadoes (NOAA Photo Library).

- Superflow is **irrotational**: superfluids can only rotate by forming a **regular array of vortices**.
- Each microscopic vortex carries a **quantum of circulation** $\kappa = h/2m \approx 2.0 \times 10^{-3}\,\mathrm{cm}^2\,\mathrm{s}^{-1}$.
- Vortices arrange themselves in a **regular array** (Abrikosov, 1957) and their circulation mimics solid-body rotation on large scales.

Mutual friction

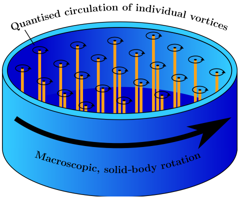

Figure 5: Regular vortex array.

- **Averaged vorticity** and **vortex area density** are

$$\boldsymbol{\omega} = 2\boldsymbol{\Omega} = \mathcal{N}_{\mathrm{v}}\kappa\hat{\boldsymbol{z}}, \quad \mathcal{N}_{\mathrm{v}} \approx 6.3 \times 10^5 \left(\frac{10\,\mathrm{ms}}{P}\right) \mathrm{cm}^{-2}. \tag{3}$$

- Angular momentum can be changed by creating (spin-up) or destroying (spin-down) vortices.

- The vortices interact with the viscous fluid component causing **mutual friction** (Hall & Vinen, 1956; Alpar, Langer & Sauls, 1984). For $\boldsymbol{\Omega} = \Omega\,\hat{\boldsymbol{\Omega}}$, the **vortex-averaged** drag force in the core is given by

$$\boldsymbol{F}_{\mathrm{mf}} = 2\mathcal{B}\rho_{\mathrm{n}}\,\hat{\boldsymbol{\Omega}} \times [\boldsymbol{\Omega} \times (\boldsymbol{v}_{\mathrm{n}} - \boldsymbol{v}_{\mathrm{e}})] + 2\mathcal{B}'\rho_{\mathrm{n}}\,\boldsymbol{\Omega} \times (\boldsymbol{v}_{\mathrm{n}} - \boldsymbol{v}_{\mathrm{e}})\,. \tag{4}$$

- The coefficients $\mathcal{B}$ and $\mathcal{B}'$ are calculated from mesoscopic **coupling physics** for a single vortex and then averaged over the full array.

(The old) type-II picture

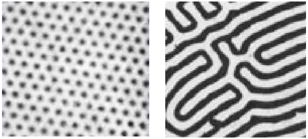

Figure 6: Type-II and intermediate type-I state (Brandt & Essmann, 1987).

- Due to high conductivity, the magnetic flux cannot be expelled from their interiors $\Rightarrow$ neutron stars do not exhibit Meissner effect and are in a **metastable** state (Baym, Pethick & Pines, 1969; Ho, Andersson & Graber, 2017).

- State depends on **characteristic lengthscales** and standard considerations give $\kappa = \lambda/\xi_{\rm ft} > 1/\sqrt{2}$ in the outer core, i.e., a **type-II state** with

$$H_{\rm c1} = 4\pi\mathcal{E}_{\rm ft}/\phi_0 \sim 10^{14}\,{\rm G}, \qquad H_{\rm c2} = \phi_0/(2\pi\xi_{\rm ft}^2) \sim 10^{15}\,{\rm G}. \tag{5}$$

- Each fluxtube carries a **flux quantum** $\phi_0 = hc/2e \approx 2.1 \times 10^{-7}\,{\rm G\,cm}^2$. All flux quanta add up to the total magnetic flux, so that the **averaged magnetic induction** is related to the fluxtube area density $\mathcal{N}_{\rm ft}$:

$$B = \mathcal{N}_{\rm ft}\phi_0, \quad \rightarrow \quad \mathcal{N}_{\rm ft} \approx 4.8 \times 10^{18}\,\left(B/10^{12}\,{\rm G}\right){\rm cm}^{-2}. \tag{6}$$

NS two-fluid model

- Macroscopic **Euler equations** for superfluid neutrons and charged fluid in zero-temperature limit (Glampedakis, Andersson & Samuelsson, 2011)

$$\left(\partial_t + v_{\rm n}^j \nabla_j\right)\left[v_{\rm n}^i + \varepsilon_{\rm n} w_{\rm np}^i\right] + \nabla^i \tilde{\Phi}_{\rm n} + \varepsilon_{\rm n} w_{\rm pn}^j \nabla^i v_j^{\rm n} = f_{\rm mf}^i + f_{\rm mag,n}^i, \tag{7}$$

$$\left(\partial_t + v_{\rm p}^j \nabla_j\right)\left[v_{\rm p}^i + \varepsilon_{\rm p} w_{\rm pn}^i\right] + \nabla^i \tilde{\Phi}_{\rm p} + \varepsilon_{\rm p} w_{\rm np}^j \nabla^i v_j^{\rm p} = -\frac{n_{\rm n}}{n_{\rm p}} f_{\rm mf}^i + f_{\rm mag,p}^i, \tag{8}$$

with $w_{\rm xy}^i \equiv v_{\rm x}^i - v_{\rm y}^i$. Modified by **new force terms**, $f_{\rm mf}^i$ and $f_{\rm mag,x}^i$, due to vortices/fluxtubes and **entrainment**, $\varepsilon_{\rm x}$ (Andreev & Bashkin, 1975).

- Supplemented by **continuity equations** and **Poisson's equation**,

$$\partial_t n_{\rm x} + \nabla_i (n_{\rm x} v_{\rm x}^i) = 0, \qquad \nabla^2 \Phi = 4\pi G \rho, \tag{9}$$

and an evolution equation for the magnetic induction B.

B-fields - Induction equation

- **Magnetic field evolution** should be related to the mechanisms affecting the fluxtubes' motion, but these are rather poorly understood (Muslimov & Tsygan, 1985; Graber, 2017, e.g.).

- It is possible to use techniques of classical magnetohydrodynamics to derive a **superconducting induction equation** (Graber et al., 2015). For the standard coupling mechanism (electron scattering), one finds:

$$\partial_t B^i \approx \epsilon^{ijk} \nabla_j \left[\epsilon_{klm} v_{\mathrm{p}}^l B^m - \frac{\kappa B}{2\pi} \frac{m}{m_{\mathrm{p}}^*} \left(\mathcal{B}' \hat{B}^l \nabla_l \hat{B}_k + \mathcal{B} \epsilon_{klm} \hat{B}^l \hat{B}^s \nabla_s \hat{B}^m \right) \right], \quad (10)$$

  with inertial, conservative (Hall-like) and dissipative (Ohmic-like) term.

- The corresponding **timescales** are too slow to drive field evolution on observable timescales, i.e., $\tau_{\mathrm{diss}} \approx 10^9$ yrs and $\tau_{\mathrm{cons}} \approx 10^{11}$ yrs.

Connection to Lab Systems

- Neutron stars contain (at least) three superfluids, characterised by large particle numbers condensed into the same quantum state. Theoretical modelling is difficult ⇒ use **laboratory counterparts** to understand them better.

- While we cannot replicate their extreme conditions, we can use the connection to known laboratory analogues to **study specific** neutron star **characteristics**.

- Many promising examples to explore this interface (Graber, Andersson & Hogg, 2017).

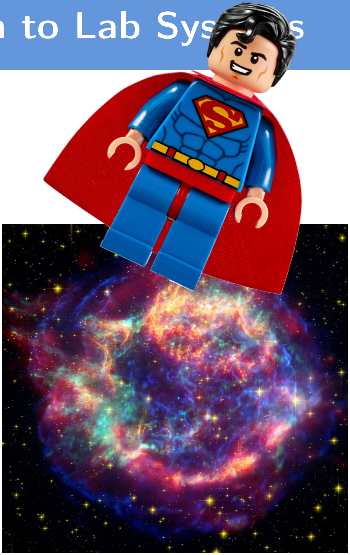

Figure 7: Cassiopeia A supernova remnant (NASA, JPL-Caltech, STScI, CXC, SAO).

Contents

Glitches Basics

- Glitches are sudden spin-ups likely caused by **angular momentum transfer** from a crustal superfluid, decoupled from the lattice (and everything tightly coupled) due to vortex pinning (Anderson & Itoh, 1975).

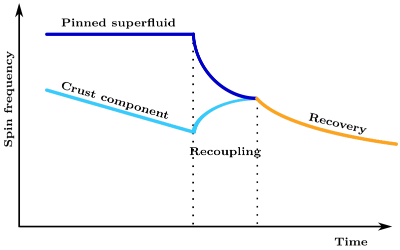

Figure 8: Sketch of an idealised glitch.

- Catastrophic unpinning triggers glitch and friction acting on **free vortices** govern **post-glitch response**.
- Models of **long-term behaviour** have been compared to observed **exponential relaxation timescales** to analyse crustal pinning forces and temperatures (Alpar et al., 1984, e.g.).

- Observations suggest that the **crust spin-up** after a glitch is very fast (Dodson, Lewis & McCulloch, 2007; Palfreyman et al., 2018).

Glitches — Modelling

- To model glitches, **decompose** star into **rigidly rotating components** coupled by friction ⇒ **predicted evolution** depends on number of components and their coupling strengths (Graber, Cumming & Andersson, 2018).

- First single-pulse observations of a Vela glitch (Palfreyman et al., 2018) allow **comparing** data and predictions ⇒ we use a **Bayesian framework** to fit models to the data (Ashton et al., 2019) to constrain the **glitch rise time** to $\lesssim$ **12.6** s and find evidence for an **overshoot** and **pre-glitch slow-down**.

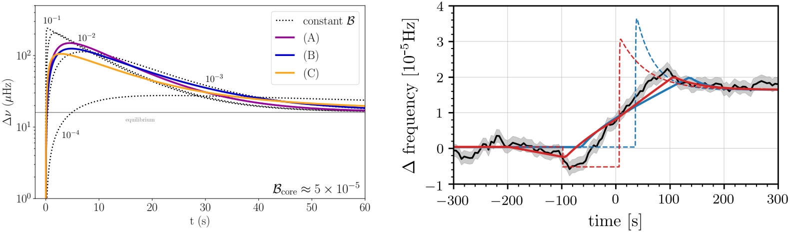

Figure 9: Glitch predictions (left) and constant ν fitted with 200 s-long sliding window to 2016 glitch (right).

Helium II spin-up

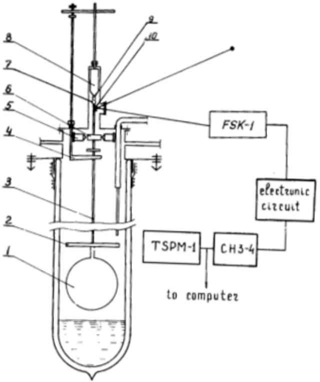

Figure 10: Schematic setup of the helium II spin-up experiments (Tsakadze & Tsakadze, 1980).

- First (and only) **systematic analysis** of rotating helium II by Tsakadze & Tsakadze (1980), shortly after first observations of **glitches** in the Vela and Crab pulsar.
- Validate presence of superfluid components in neutron stars by measuring **relaxation timescales** after initial changes in the container's rotation.
- Performed for various temperatures, vessel configurations and rotational properties.
- Model comparison is hard (Reisenegger, 1993; van Eysden & Melatos, 2011).

Helium II glitches

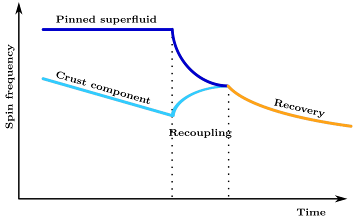

Figure 11: Sketch of an idealised neutron star glitch.

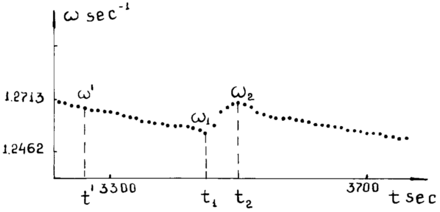

Figure 12: Measurement of a laboratory glitch.

- **Glitches** are not only detected in neutron stars, but have also been observed in helium experiments (Tsakadze & Tsakadze, 1980). This supports the idea that they are caused by an **internal superfluid reservoir**.
- There is **only one (!!)** observation of a helium II glitch. Updated experiments could help to understand aspects such as the trigger.

Glitches — Crust-core interface

- One of the important unknowns in modelling glitches is the role of the **crust-core interface**, i.e., how do the two superfluid regions transition into each other ⇒ Can we investigate this with helium?

- Helium-3 becomes superfluid below 3 mK. The transition is different to bosonic helium II because helium-3 atoms are fermions and have to form **Cooper-pairs** as expected for the neutron star interior.

- The pairing occurs in a spin-triplet, *p*-wave state: the Cooper pairs have internal structure resulting in **3 superfluid phases** (Vollhardt, 1998).

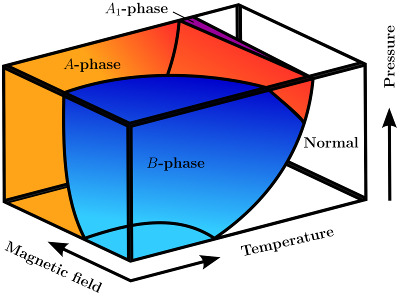

Figure 13: Schematic phase diagram of helium-3.

Helium-3 interfaces

- **B-phase** behaves similar to helium II and crustal superfluid; **A-phase** exhibits anisotropic behaviour and resembles core neutron superfluid.

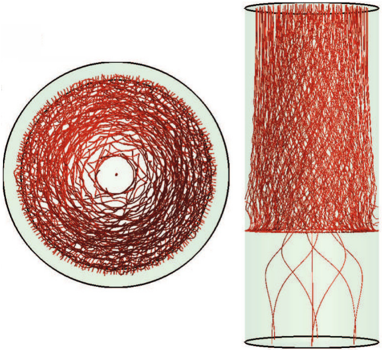

Figure 14: Vortex-line simulation for spin-down of two-phase helium-3 (Walmsley et al., 2011).

- Study vortices across an interface with rotating **two-phase samples** (different $\mathcal{B}$, $\mathcal{B}'$) using NMR measurements and modern vortex-line simulations (Walmsley et al., 2011).
- Interface strongly modifies dynamics:
  - **Vortex sheet** formation
  - **Vortex tangle** forms in B-phase, reconnections increase dissipation
  - **Differential rotation**
- Interface can become unstable to Kelvin-Helmholtz instability (Finne et al., 2006).

Contents

Superconductors

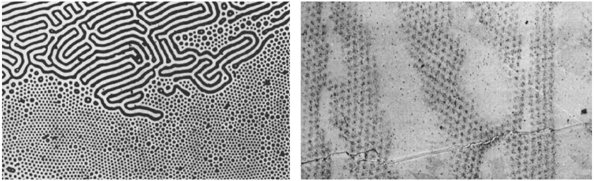

Figure 15: Intermediate state of type-I and type-II phases (Brandt & Essmann, 1987; Essmann, 1971).

- For laboratory systems, experiments and numerical calculations complement each other $\Rightarrow$ account for pinning defects, bending, long-range repulsion and reconnections in **time-dependent Ginzburg-Landau models**.
- Our understanding of **macroscopic NS superconductivity** is based on **time-independent equilibrium** and **single-component considerations**. It is unclear what happens as the star cools below $T_{\rm c}$ and when entrainment is included $\Rightarrow$ how can we better understand the phase transition?

SC formation

- In the outer core, initially, only protons are superconducting (neutrons remain normal), so we model the **formation of the superconducting phase** with a single-component time-dependent Ginzburg-Landau model.

- Study the **dynamics of the phase transition** under different circumstances in analogy to numerical experiments of laboratory systems (Liu, Mondello & Goldenfeld, 1991; Frahm, Ullah & Dorsey, 1991).

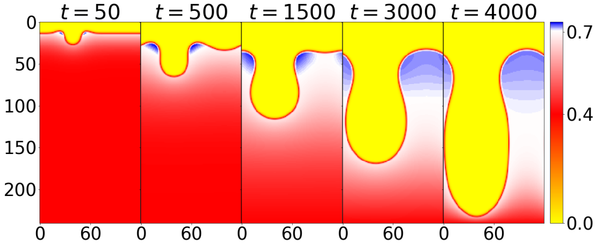

Figure 16: Evolution of the magnetic field in a type-I system in the nucleation regime.

Micro-scale model

- Nucleons are strongly coupled via non-dissipative **entrainment**, which affects the superconductor ⇒ use a zero-temperature, **two-component** Ginzburg-Landau model and extend earlier works to be Galilean invariant.
- Aim is to construct **phase diagrams** and deduce the protons' state for different EoSs as a function of the density (Wood & Graber, in preparation).

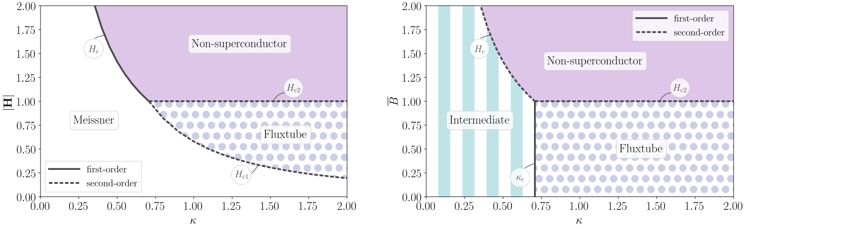

Figure 17: Phase diagrams for a one-component superconductor, for different values of the Ginzburg-Landau parameter, κ. The experiment with an imposed external field, $|\mathbf{H}|$, in nondimensional units is shown on the left, while the right panel shows the phase transitions in the experiment with an imposed mean flux, $\overline{B}$.

Core SC

Preliminary results

- Entrainment causes behaviour similar to **type-1.5 superconductivity** due to fluxtube repulsion on short scales and attraction on large scales $\Rightarrow$ when imposing $\overline{B}$, mixed states appear.

- For typical EoSs, the outer core is no longer a type-II superconductor but a type-1.5 system $\Rightarrow$ **magnetic flux is irregularly distributed and retained**.

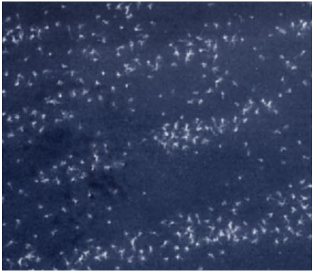

Figure 18: Magnetic decoration image of multi-band superconductor Mg2B (Moshchalkov et al., 2009).

- This could affect the neutron star's large-scale magnetism, but to really translate between our microscale model and a magneto-hydrodynamical description, we need to find a way to include the **normal electrons**.

Conclusions

- Neutron stars are expected to contain (at least) **three distinct quantum condensates** that influence the stars' macroscopic behaviour. The majority of our knowledge of these superfluids originates from theoretical work on their laboratory counterparts.
- As significant progress has been made in understanding laboratory condensates in recent years, there are many exciting ways to **combine both fields** and study neutron star astrophysics in light of terrestrial experiments and theoretical frameworks.
- Promising approaches include the study of **pulsar glitches**, which are a direct manifestation of macroscopic neutron superfluidity, and analysing the microphysics of the **superconducting phase transition** and the impact on the neutron star magnetism.

Thank you.

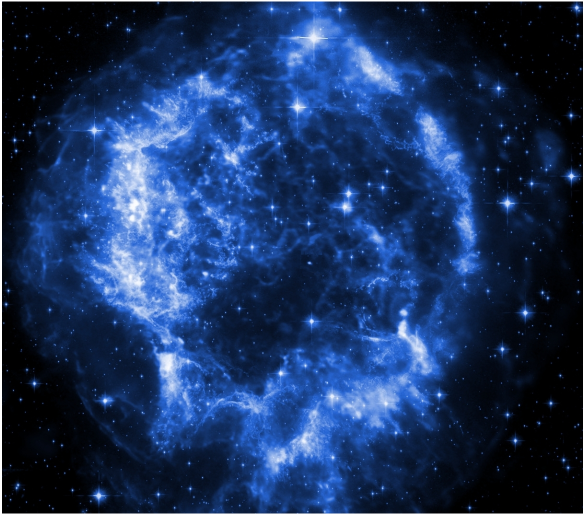

$P\dot{P}$-diagram

- The $P\dot{P}$-diagram is a great diagnostic tool to analyse pulsar physics. Characteristic ages and magnetic field strengths are estimated as

$$\tau_c \sim 0.5\, P\dot{P}^{-1}, \qquad B \sim 3.2 \times 10^{19} (P\dot{P})^{1/2}\,\mathrm{G}. \tag{11}$$

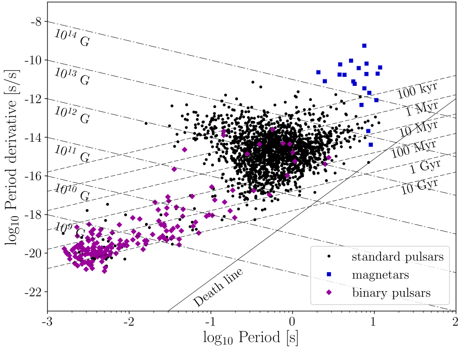

Figure 19: $P\dot{P}$-diagram for $\sim$ 2500 known radio pulsars from the ATNF pulsar catalogue, which can be found at `http://www.atnf.csiro.au/people/pulsar/psrcat/`. Different classes of neutron stars are highlighted including standard rotation-powered pulsars, magnetars and binary pulsars.

Appendix

NS mutual friction

- Different processes affect **vortex dynamics** in the crust and the core:
  - phonon excitations (Jones, 1990)
  - Kelvin wave excitations (Epstein & Baym, 1992; Jones, 1992)
  - electron quasi-particle scattering (Feibelman, 1971)
  - electrons scatter off vortex field (Alpar, Langer & Sauls, 1984; Andersson, Sidery & Comer, 2006)
  - Kelvin wave excitations (Link, 2003)

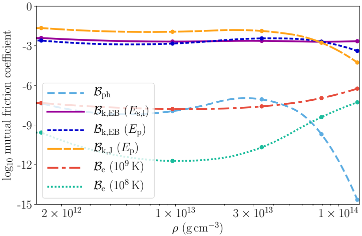

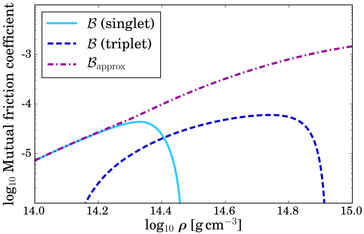

Figure 20: Mutual friction strength in the crust (left) for the composition of Negele & Vautherin (1973) and realistic vortex-lattice interaction parameters (Epstein & Baym, 1992; Donati & Pizzochero, 2006) and core (right) for NRAPR (Steiner et al., 2005) and parametrised neutron gaps (Ho, Glampedakis & Andersson, 2012).

Appendix

Glitch model

- **Decompose** the neutron star into crust superfluid, core superfluid and a non-superfluid 'crust' component. The latter two rotate rigidly and are coupled via a constant mutual friction coefficient $\mathcal{B}_{\rm core} \approx 5 \times 10^{-5}$.

- Neglecting entrainment for simplicity, the **equations of motion** are

$$\dot{\Omega}_{\rm sf} = \mathcal{B}_{\rm crust} \left[2\Omega_{\rm sf} + \tilde{r} \frac{\partial \Omega_{\rm sf}}{\partial \tilde{r}} \right] (\Omega_{\rm crust} - \Omega_{\rm sf}), \tag{12}$$

$$\dot{\Omega}_{\rm core} = \mathcal{B}_{\rm core} 2\Omega_{\rm core} (\Omega_{\rm crust} - \Omega_{\rm core}), \tag{13}$$

$$\dot{\Omega}_{\rm crust} = -\frac{N_{\rm ext}}{I_{\rm crust}} - \frac{I_{\rm core}}{I_{\rm crust}} \dot{\Omega}_{\rm core} - \frac{1}{I_{\rm crust}} \int \rho \tilde{r}^2 \dot{\Omega}_{\rm sf} \, \mathrm{d}V. \tag{14}$$

- Relate ρ and $\tilde{r}$ in the crust by solving the **TOV equations** for a realistic EoS to obtain $\mathcal{B}_{\rm crust}(\tilde{r})$ and integrate (12)-(14) in cylindrical geometry for **Vela pulsar** parameters ($\Omega_{\rm crust}(0) \approx 70\,\mathrm{Hz}$, $\Delta\Omega_{\rm crit} \approx 10^{-2}\,\mathrm{Hz}$) for $120\,\mathrm{s}$.

Crustal evolution

- Compare different **friction profiles** by computing the change in crust frequency $\Delta\nu$. Glitch-rise shape depends crucially on **relative strength** of crust and core mutual friction (Graber, Cumming & Andersson, 2018).
- With $\mathcal{B}_{\rm core} \sim 5 \times 10^{-5}$, the crust coupling is faster than core coupling, creating a characteristic **overshoot** feature. The onset of crust-core coupling is visible as a break in the **phase shift** ϕ and timing residuals.

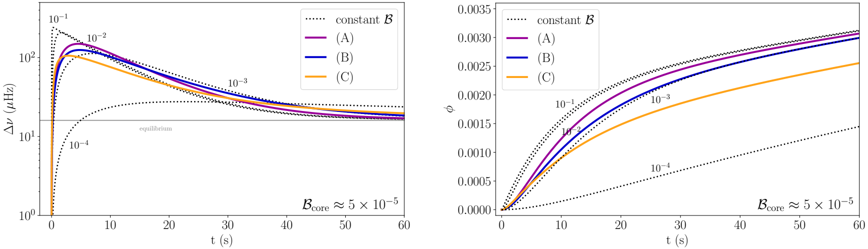

Figure 21: Change in crustal frequency $\Delta\nu(t) = [\Omega_{\rm crust}(t) - \Omega_{\rm crust}(0)]/2\pi$ and phase shift $\phi = \int \Delta\nu \, {\rm d}t$.

Appendix

Glitch data comparison I

- First single-pulse observations of a glitch in the Vela pulsar (Palfreyman et al., 2018) allow a **comparison** between the data and predictions.
- Use a **Bayesian framework** to fit phenomenological models of the star's rotation frequency to the Vela pulsar data (Ashton et al., 2019). This allows to constrain the **glitch rise time** to less than **12.6** s with 90% confidence.

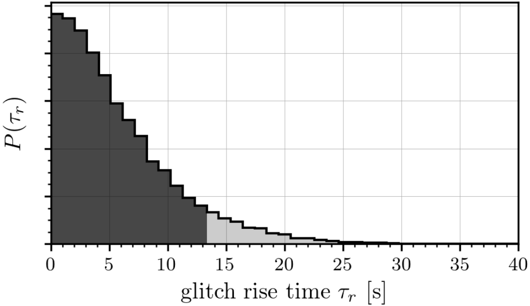

Figure 22: Posterior distribution for the rise time of the glitch. The rise time is the free time scale in a two-component neutron star model. The dark shaded region marks the 90% confidence interval.

Glitch data comparison II

- We find definite evidence for an **overshoot** and fast decay timescale $\sim 55\,\mathrm{s} \Rightarrow$ requires three components in a body-averaged formalism.
- We find evidence for a **slow-down** of the star's rotation immediately prior to the glitch $\Rightarrow$ some **noise** process may trigger the glitch by causing a **critical lag** between crustal superfluid and the lattice.

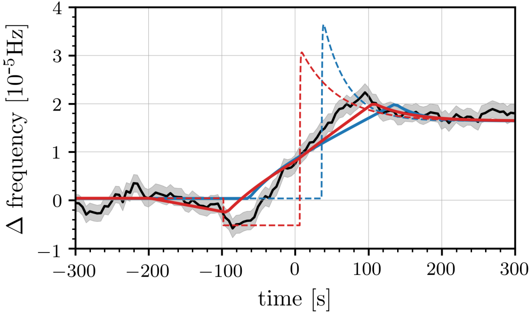

Figure 23: Frequency evolution during the 2016 Vela glitch: constant frequency model fitted with 200 s-long sliding window with 90% confidence interval (grey) plus maximum-likelihood fits for the overshoot (blue) and slow-down+overshoot (red) models. Dashed curves show the raw frequency evolution, while the solid ones show the time-averaged frequency evolution.

Galilean invariant GL model

- With entrainment, velocity-dependent terms in energy density must read

$$F_{\mathsf{vel}} = \tfrac{1}{2}\rho_{\rm p}|\mathbf{V}_{\rm p}|^2 + \tfrac{1}{2}\rho_{\rm n}|\mathbf{V}_{\rm n}|^2 - \tfrac{1}{2}\rho^{\rm pn}|\mathbf{V}_{\rm p} - \mathbf{V}_{\rm n}|^2\,, \tag{15}$$

where $\rho_{\rm p}$ and $\rho_{\rm n}$ are the true mass densities, the coefficient $\rho^{\rm pn} < 0$ determines the strength of entrainment (Andreev & Bashkin, 1975) and $\mathbf{V}_{\rm p,n}$ are superfluid velocities related to the canonical momenta.

- In the mean-field framework, entrainment first enters at 4th order in $\psi_{\rm n,p}$ and 2nd order in their derivatives, i.e., we require a linear combination of

$$|\psi_x|^2|\boldsymbol{\nabla}\psi_y|^2,\ \psi_x\psi_y\boldsymbol{\nabla}\psi_x^\star\cdot\boldsymbol{\nabla}\psi_y^\star,\ \psi_x\psi_y^\star\boldsymbol{\nabla}\psi_x^\star\cdot\boldsymbol{\nabla}\psi_y,\ \psi_x^\star\psi_y^\star\boldsymbol{\nabla}\psi_x\cdot\boldsymbol{\nabla}\psi_y, \tag{16}$$

where $x, y \in \{\rm p, n\}$. The result can be linked to the **Skyrme model**, to deduce equation-of-state dependent coefficients.

Helmholtz free energy density

- Total Helmholtz free energy density is obtained by adding entrainment terms to the usual free energy of a two-component superfluid, and introducing the magnetic vector potential **A** by **minimal coupling**:

$$
\begin{aligned}
F[\psi_\mathrm{p},\psi_\mathrm{n},\mathbf{A}] = {} & F_0 - \mu_\mathrm{p}|\psi_\mathrm{p}|^2 - \mu_\mathrm{n}|\psi_\mathrm{n}|^2 + \frac{g_\mathrm{pp}}{2}|\psi_\mathrm{p}|^4 + \frac{g_\mathrm{nn}}{2}|\psi_\mathrm{n}|^4 + g_\mathrm{pn}|\psi_\mathrm{p}|^2|\psi_\mathrm{n}|^2 \\
& + \frac{\hbar^2}{4m_\mathrm{u}}\left|\left(\boldsymbol{\nabla} - \frac{2ie}{\hbar c}\mathbf{A}\right)\psi_\mathrm{p}\right|^2 + \frac{\hbar^2}{4m_\mathrm{u}}|\boldsymbol{\nabla}\psi_\mathrm{n}|^2 + \frac{1}{8\pi}|\boldsymbol{\nabla}\times\mathbf{A}|^2 \\
& + h_1\left|\left(\boldsymbol{\nabla} - \frac{2ie}{\hbar c}\mathbf{A}\right)(\psi_\mathrm{n}^\star\psi_\mathrm{p})\right|^2 + \tfrac{1}{2}(h_2 - h_1)\boldsymbol{\nabla}(|\psi_\mathrm{p}|^2)\cdot\boldsymbol{\nabla}(|\psi_\mathrm{n}|^2) \\
& + \tfrac{1}{4}h_3\left(\left|\boldsymbol{\nabla}(|\psi_\mathrm{p}|^2)\right|^2 + \left|\boldsymbol{\nabla}(|\psi_\mathrm{n}|^2)\right|^2\right), \qquad (17)
\end{aligned}
$$

where F_0 is an arbitrary reference level and proton Cooper pairs have charge $2\mathrm{e}$. μ_p and μ_n are the chemical potentials, while g_pp and g_nn define the self-repulsion of the condensates, and g_pn their mutual repulsion.

Thought experiments

- To find the **ground state** for our system in the presence of an **imposed magnetic field**, we can perform two distinct experiments: we control (i) the magnetic flux density, $\mathbf{B} = \boldsymbol{\nabla} \times \mathbf{A}$, by imposing a mean or net magnetic flux, or (ii) the thermodynamic external magnetic field, $\mathbf{H}$.

- In the first case, we minimise the **Helmholtz free energy**, $\mathcal{F} = \langle F \rangle$, where the angled brackets represent some kind of integral over our physical domain $\Rightarrow$ closely approximates the conditions in the neutron star core, which becomes superconducting as the star cools in the presence of pre-existing magnetic field. The ground state can be **inhomogeneous**.

- In the second case, we minimise the dimensionless **Gibbs free energy**, $\mathcal{G} = \mathcal{F} - 2\kappa^2 \mathbf{H} \cdot \langle \mathbf{B} \rangle$. In an unbounded domain, the ground state is guaranteed to be **homogeneous**, and the phase diagram simpler.

Euler-Lagrange equations

- Whether we work with $\mathcal{F}$ or $\mathcal{G}$, we obtain the same equations of motion:

$$\kappa^2 \boldsymbol{\nabla} \times (\boldsymbol{\nabla} \times \mathbf{A}) = \Im \left\{ \psi_\mathrm{p}^\star (\boldsymbol{\nabla} - \mathrm{i}\mathbf{A}) \psi_\mathrm{p} + \frac{h_1}{\epsilon} \psi_\mathrm{n} \psi_\mathrm{p}^\star (\boldsymbol{\nabla} - \mathrm{i}\mathbf{A}) (\psi_\mathrm{n}^\star \psi_\mathrm{p}) \right\} , \tag{18}$$

$$\begin{aligned} \nabla^2 \psi_\mathrm{n} &= R^2 (|\psi_\mathrm{n}|^2 - 1) \psi_\mathrm{n} + \alpha (|\psi_\mathrm{p}|^2 - 1) \psi_\mathrm{n} \\ &\quad - h_1 \psi_\mathrm{p} (\boldsymbol{\nabla} + \mathrm{i}\mathbf{A})^2 (\psi_\mathrm{p}^\star \psi_\mathrm{n}) \\ &\quad - \psi_\mathrm{n} \nabla^2 \left(\frac{h_2 - h_1}{2} |\psi_\mathrm{p}|^2 + \frac{h_3}{2\epsilon} |\psi_\mathrm{n}|^2 \right) , \end{aligned} \tag{19}$$

$$\begin{aligned} (\boldsymbol{\nabla} - \mathrm{i}\mathbf{A})^2 \psi_\mathrm{p} &= (|\psi_\mathrm{p}|^2 - 1) \psi_\mathrm{p} + \frac{\alpha}{\epsilon} (|\psi_\mathrm{n}|^2 - 1) \psi_\mathrm{p} \\ &\quad - \frac{h_1}{\epsilon} \psi_\mathrm{n} (\boldsymbol{\nabla} - \mathrm{i}\mathbf{A})^2 (\psi_\mathrm{n}^\star \psi_\mathrm{p}) \\ &\quad - \psi_\mathrm{p} \nabla^2 \left(\frac{h_2 - h_1}{2\epsilon} |\psi_\mathrm{n}|^2 + \frac{h_3}{2} |\psi_\mathrm{p}|^2 \right) . \end{aligned} \tag{20}$$

Appendix

Energy per flux quantum

- We solve the Euler-Lagrange equations with **quasi-periodic boundary conditions** (Wood et al., 2019), which involves specifying the domain size $L_x \times L_y$, and the number N of magnetic flux quanta within the domain $\Rightarrow$ different choices allow comparing **square** and **hexagonal lattices**.

- The Helmholtz free energy per magnetic flux quantum per unit length is

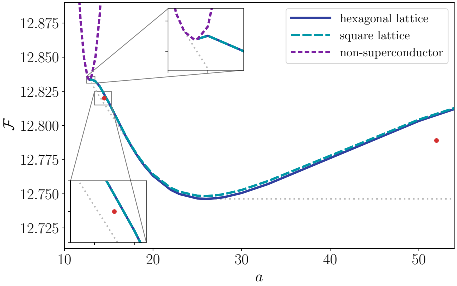

$$\mathcal{F} \equiv \frac{1}{N} \int_{x=0}^{L_x} \int_{y=0}^{L_y} F \, \mathrm{d}x \, \mathrm{d}y \,. \tag{21}$$

Figure 24: Helmholtz free energy per flux quantum per unit length, $\mathcal{F}$, as a function of the area per magnetic flux quantum, $a = 2\pi/\overline{B}$, for the NRAPR EoS at $n_\mathrm{b} = 0.2831/\mathrm{fm}^3$. The energy in the square (long-dashed, cyan) and hexagonal (solid, blue) lattice states matches smoothly onto the energy of the non-superconducting state (short-dashed, purple) at $a \simeq 12.9$.

Inhomogeneous ground-states

- Choosing a sufficiently large domain, and values of a, we otain examples of **inhomogeneous ground states** $\Rightarrow$ for NRAPR at $n_{\mathrm{b}} = 0.2831/\mathrm{fm}^3$ with $a = 14.5$ plus $N = 24$ (left) and $a = 52$ plus $N = 14$ (right).

- In both cases, the **aspect ratio** is $\sqrt{3}$ and the pure hexagonal lattice a possible state but not the ground state $\Rightarrow$ $\mathcal{F}$ is lower than for pure lattice.

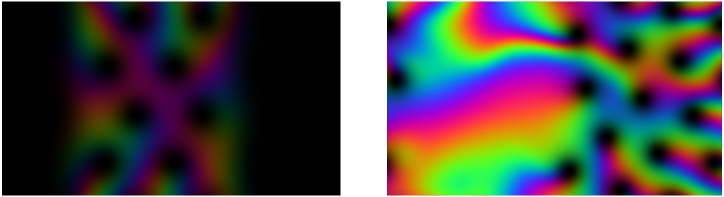

Figure 25: Inhomogeneous groundstates for NRAPR. Brightness and hue indicate density and phase of the proton order parameter, ψ_{p}, respectively. The left panel shows a mixture of non-superconducting protons and hexagonal fluxtube lattice, while the right one is mixture of Meissner state and hexagonal fluxtube lattice.

Example phase diagrams

- When mixed states are present, second-order phase transitions are replaced by **first-order transitions** at $H_{c1'} < H_{c1}$ and $H_{c2'} > H_{c2}$.

- We can determine **critical fields** (partially semi-analytically, partially numerically) and construct phase-diagrams of the superconducting state throughout the neutron star core. For the **LNS** equation of state:

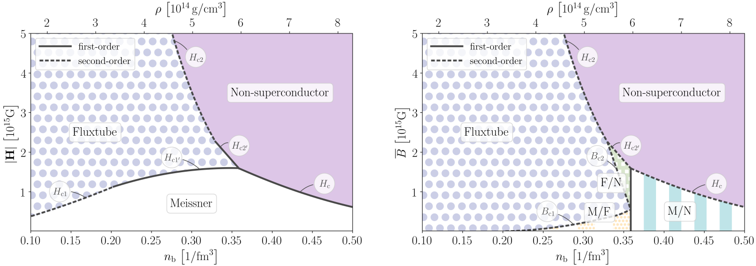

Figure 26: Phase diagrams for LNS. There are inhomogeneous regimes of the Meissner/Non-superconducting (M/N), Meissner/Fluxtube (M/F) and Fluxtube/Non-superconducting (F/N) states.

Ultra-cold gases

- A BEC of **weakly-interacting bosons** was first realised by cooling Rubidium atoms to $T \sim$ nK (Anderson et al., 1995; Davis et al., 1995), and the superfluid transition observed shortly after (Matthews et al., 1999; Madison et al., 2000).

- Although the field is relatively young, ultra-cold gases provide **many possibilities** to study superfluidity: e.g. fermionic gases, two-component systems, optical lattices, etc.

- Very simple advantage: **absorption imaging** of clouds is a great tool to study behaviour of individual vortices.

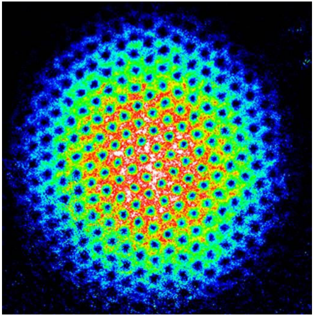

Figure 27: Vortex array in a rotating, dilute BEC of Rubidium atoms (Engels et al., 2002).

Appendix

GPE modelling

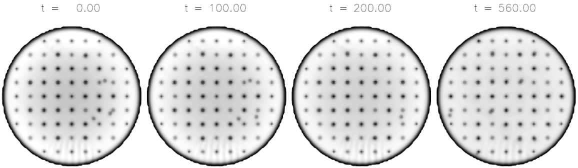

Figure 28: Snapshots of superfluid density during the spin-down of a BEC (Warszawski & Melatos, 2012).

- Time evolution of the **Gross-Pitaevskii equation** describes vortex motion ⇒ use this approach to study the pinned **crustal superfluid** in neutron stars (Warszawski & Melatos, 2012).
- Collective vortex motion in the presence of pinning potential can cause **glitch-like events** ⇒ study the unknown trigger and glitch statistics.
- **Two-component GP** formalisms have been used to study neutron star core properties (Alford & Good, 2008; Drummond & Melatos, 2017, e.g.).

References I

Abrikosov A. A., 1957, JPCS, 2, 199

Alford M. G., Good G., 2008, PhRvB, 78, 024510

Alpar M. A., Anderson P. W., Pines D., Shaham J., 1984, ApJ, 278, 791

Alpar M. A., Langer S. A., Sauls J. A., 1984, ApJ, 282, 533

Anderson M. H., Ensher J. R., Matthews M. R., Wieman C. E., Cornell E. A., 1995, Sci, 269, 198

Anderson P. W., Itoh N., 1975, Natur, 256, 25

Andersson N., Sidery T., Comer G. L., 2006, MNRAS, 368, 162

Andreev A. F., Bashkin E. P., 1975, JETP, 42, 164

Ashton G., Lasky P. D., Graber V., Palfreyman J., 2019, Nat. Astron., 3, 1143

Bardeen J., Cooper L. N., Schrieffer J. R., 1957, PhRv, 108, 1175

Baym G., Pethick C. J., Pines D., 1969, Natur, 224, 673

Brandt E. H., Essmann U., 1987, PSSBR, 144, 13

Chamel N., 2008, MNRAS, 388, 737

Davis K., Mewes M.-O., Andrews M. R., van Druten N. J., Durfee D. S., Kurn D. M., Ketterle W., 1995, PhRvL, 75, 3969

Dodson R., Lewis D., McCulloch P., 2007, Ap&SS, 308, 585

Donati P., Pizzochero P. M., 2006, PhLB, 640, 74

Drummond L. V., Melatos A., 2017, MNRAS, 472, 4851

Engels P., Coddington I., Haljan P. C., Cornell E. A., 2002, PhRvL, 89, 100403

Epstein R. I., Baym G., 1992, ApJ, 387, 276

Essmann U., 1971, Phy, 55, 83

References II

Finne A. P., Eltsov V. B., Hänninen R., Kopnin N. B., Kopu J., Krusius M., Tsubota M., Volovik G. E., 2006, RPPh, 69, 3157

Frahm H., Ullah S., Dorsey A. T., 1991, PhRvL, 66, 3067

Glampedakis K., Andersson N., Samuelsson L., 2011, MNRAS, 410, 805

Graber V., 2017, AN, 338, 1090

Graber V., Andersson N., Glampedakis K., Lander S. K., 2015, MNRAS, 453, 671

Graber V., Andersson N., Hogg M., 2017, IJMPD, 26, 1730015

Graber V., Cumming A., Andersson N., 2018, ApJ, 865, 23

Hall H. E., Vinen W. F., 1956, PSPSA, 238, 215

Ho W. C. G., Glampedakis K., Andersson N., 2012, MNRAS, 422, 2632

Ho W. W. C. G., Andersson N., Graber V., 2017, PhRvC, 96, 065801

Jones P. B., 1990, MNRAS, 243, 257

Jones P. B., 1992, MNRAS, 257, 501

Link B., 2003, PhRvL, 91, 101101

Liu F., Mondello M., Goldenfeld N., 1991, PhRvL, 66, 3071

Madison K., Chevy F., Wohlleben W., Dalibard J., 2000, PhRvL, 84, 806

Matthews M. R., Anderson B. P., Haljan P. C., Hall D. S., Wieman C. E., Cornell E. A., 1999, PhRvL, 83, 2498

Migdal A. B., 1959, NucPh, 13, 655

Moshchalkov V. V. et al., 2009, PhRvL, 102, 117001

Muslimov A. G., Tsygan A. I., 1985, SvA, 11, 80

References III

Palfreyman J., Dickey J. M., Hotan A., Ellingsen S., van Straten W., 2018, Natur, 556, 219

Reisenegger A., 1993, JLTP, 92, 77

Steiner A. W., Prakash M., Lattimer J. M., Ellis P. J., 2005, PhR, 411, 325

Tsakadze J. S., Tsakadze S. J., 1980, JLTP, 39, 649

van Eysden C. A., Melatos A., 2011, JLTP, 165, 1

Vollhardt D., 1998, in Pair Correlations in Many-Fermion Systems, Kresin V. Z., ed., Springer US, Boston, MA, pp. 205–220

Walmsley P. M., Eltsov V. B., Heikkinen P. J., Hosio J. J., Hänninen R., Krusius M., 2011, PhRvB, 84, 184532

Warszawski L., Melatos A., 2012, MNRAS, 423, 2058

Wood T. S., Mesgarnezhad M., Stagg G. W., Barenghi C. F., 2019, PhRvB, 100, 024505